# Impacts of seasonal transitions of ENSO on atmospheric river activity over East Asia

**Moeka NAOI**

*Graduate School of Life and Environmental Sciences, University of Tsukuba, Tsukuba, Japan*

**Youichi KAMAE*, Hiroaki UEDA**

*Faculty of Life and Environmental Sciences, University of Tsukuba, Tsukuba, Japan*

**and**

**Wei MEI**

*Department of Marine Sciences, University of North Carolina at Chapel Hill, Chapel Hill, USA*

------------------------------------

*) Corresponding author: Youichi Kamae, Faculty of Life and Environmental Sciences, University of Tsukuba, 1-1-1 Tennoudai, Tsukuba, Ibaraki 305-8572, JAPAN
Email: kamae.yoichi.fw@u.tsukuba.ac.jp
Tel: +81-29-853-5878
Fax: +81-29-853-6709

## Abstract

Atmospheric rivers (ARs), narrow water vapor transport bands over the mid-latitudes, often cause great socio-economic impacts over East Asia. While it has been shown that summertime AR activity over East Asia is strongly induced by preceding-winter El Niño development, it remains unclear the extent to which seasonal transitions of El Niño Southern Oscillation (ENSO) from winter to summer affect the AR activity. Here we examine the relationship between the seasonal transitions of ENSO and the summertime AR activity over East Asia using an atmospheric reanalysis and high-resolution atmospheric general circulation model (AGCM) ensemble simulations. A rapid transition from preceding-winter El Niño to summertime La Niña results in more AR occurrence over northern East Asia via northward expansion of an anomalous low-level anticyclone over the western North Pacific compared to sustained or decayed El Niño cases. The northward expansion of the anticyclone is consistent with a steady response of the atmosphere to the anomalous condensation heating over the Maritime Continent and equatorial Pacific. Meridional positions of the extratropical AR occurrence and circulation anomalies are different between the reanalysis and AGCM simulations, which is possibly contributed by a limited sample size and/or AGCM biases and suggests that seasonal prediction of AR-related natural disaster risk over East Asia on a regional scale remains a challenge.

**Keywords** ENSO; atmospheric river; East Asia, western North Pacific subtropical high

## 1. Introduction

Atmospheric rivers (ARs), narrow moisture transport bands developing over the mid-latitudes, have been extensively studied (e.g. Guan and Waliser 2015; Gimeno et al. 2016; Shields et al. 2018; American Meteorological Society 2019) because of their great impacts on society through heavy rainfall and associated natural disasters (e.g. Ralph et al. 2011; Gimeno et al. 2014; Waliser and Guan 2017). The regional occurrence of ARs is highly dependent on seasons, especially in the northeastern and southeastern Pacific, East and South Asia, and the Middle East (Guan and Waliser 2015). Over East Asia, frequent AR genesis especially during summer (Guan and Waliser 2019) often causes extreme rainfall events (Kamae et al. 2017b, c). For example, ARs contribute to heavy rainfall events of August 2014 (Hirota et al. 2016; Tsuji and Takayabu 2019) and July 2018 (Shimpo et al. 2019; Takemura et al. 2019; Tsuguti et al. 2019), which killed 75 and 237 people, respectively.

Recently, interannual variations and future changes in AR occurrence frequency over East Asia have been studied using atmospheric reanalyses and model simulations. Kamae et al. (2017b) found that summertime AR frequency over East Asia tends to increase following wintertime El Niño development with a half-year lag. A key factor connecting El Niño-Southern Oscillation (ENSO) and the East Asian AR frequency is the western North Pacific subtropical high (WNPSH). The local effect of concurrent cold anomaly in underlying sea surface temperature (SST; Wang et al. 2000) and the delayed effect of the North Indian

Ocean and South China Sea warming after the wintertime El Niño intensify the WNPSH by increasing surface divergence over the western subtropical Pacific (Xie et al. 2009, 2016). Through this “Indian-western Pacific Ocean Capacitor (IPOC)” effect, AR frequency is increased on the northwestern flank of the anomalous WNPSH in post El Niño summers (Kamae et al. 2017b). Kamae et al. (2019) further pointed out that the Indo-Pacific SST is also the key to future projections of East Asia-western North Pacific AR frequency by analyzing atmospheric general circulation model (AGCM) simulations forced by different SST warming patterns. An increase in atmospheric water vapor under global warming results in an increase in AR frequency over the Northern Hemisphere mid-latitudes (see also Espinoza et al. 2018). In addition, warmer Indian Ocean and South China Sea are responsible for a larger increase in East-Asian ARs via favoring an anomalously strong WNPSH and southwesterly anomalies on its northwestern flank (Kamae et al. 2019).

In contrast to the IPOC effect, summertime AR response over the western North Pacific to the concurrent anomaly in the equatorial Pacific SST has not been well understood. Mundhenk et al. (2016) examined summertime ENSO impact by compositing El Niño and La Niña years and concluded that ENSO has no systematic effects on East Asian ARs (Fig. 8a, c in Mundhenk et al. 2016). This is partly due to limited sample size: reanalysis data used in this study only cover 36 years (i.e., 1979–2014). In contrast, Kamae et al. (2019) pointed out that summertime cool SST anomaly over the equatorial Pacific dominates the second leading mode of the interannual variations in summertime

East-Asian AR frequency in a set of 10-member ensemble AGCM simulations. They suggested that the summertime La Niña-like SST anomaly may modulate the East Asian AR frequency via changing North Pacific atmospheric circulation (Wang et al. 2013; Paek et al. 2019). However, the physical connection between the summertime La Niña and the East Asian AR activity has not been systematically explored.

In the present study, the importance of summertime Pacific SST forcing to the East Asian AR frequency is studied using an atmospheric reanalysis and numerical simulations. Atmospheric and oceanic observations of the recent decades indicate that ENSO exhibits asymmetries in strength, duration and transition (Stein et al. 2010 and references therein). Strong El Niño developed during winter (sometimes called “super El Niño”), for example in 1997/1998 or 2015/2016, rapidly decays after spring and tends to show a rapid transition to La Niña. In contrast, La Niña tends to have moderate strength and longer duration than El Niño. In this study, the relationship between the seasonal development/transition of ENSO and the summertime AR frequency over East Asia and the physical mechanisms responsible for the relationship are examined. We use both an atmospheric reanalysis and an ensemble of high-resolution AGCM simulations to increase the sample size and to assess the robustness of the results. This paper is organized as follows. Section 2 describes data and methods including an atmospheric reanalysis, model simulations, and AR detection method. Section 3 compares summertime AR frequency over the North Pacific among different ENSO transitions from winter to summer. In section 4, we examine the possible importance of the tropical atmospheric heating/cooling anomalies related to ENSO transitions to the mid-latitude AR frequency. Section 5 presents a summary and discussion.

## 2. Data and methods

### *2.1 Observations, reanalysis, and ENSO classification*

We use the Japanese 55-year Reanalysis (JRA-55; Kobayashi et al. 2015) at 1.25° × 1.25° spatial resolution to examine the historical variations in AR frequency and related atmospheric fields. The SST data used in this study are COBE-SST2 (Hirahara et al. 2014) which were used in the ensemble simulations described in section 2.2 as a boundary condition. The spatial resolution of this SST data set is 1.0° × 1.0°. To compare with the results of the ensemble simulations detailed in section 2.2, we examine the AR frequency during 1958–2010.

We divided 53 years into nine groups based on seasonal ENSO transition: combinations of preceding boreal-winter El Niño, neutral, and La Niña, and concurrent boreal-summer El Niño, neutral, and La Niña. Table 1 shows a summary of the clustering. Based on SST anomaly over Niño3 domain (150°–90°W; 5°S–5°N), years with December-to-February (DJF)-mean anomaly larger than 1 K compared to the climatology (1958–2010) are defined as El Niño (> 1 K) or La Niña (< −1 K) winters. Totally there are 7 La Niña, 8 El Niño, and 38 neutral winters during 1958–2010 (Table 1). Similarly, June-to-August (JJA) SST anomaly is used for summertime clustering. During summer, the SST threshold used for classification is 0.5 K (> 0.5 K and < –0.5 K for El Niño and La Niña summers, respectively) because in this season Niño3 SST exhibits smaller variability than in boreal winter (Stein et al. 2010). Numbers of obtained La Niña, neutral, and El Niño summers are 14, 26, and 13, respectively (Table 1). Figure 1 shows the composite mean SST anomaly compared to the climatology. In addition to the summertime ENSO signals, lagged effects of wintertime ENSO are also found: for example, SSTs over the North Indian Ocean and South China Sea tend to be higher (lower) after wintertime El Niño (La Niña), consistent with the IPOC effect (Xie et al. 2009, 2016). The sustained ENSO years and ENSO transition years have limited samples (1, 2, 1 and 2 for sustained La Niña, sustained El Niño, La Niña-to-El Niño transition, and El Niño-to-La Niña transition years, respectively), suggesting difficulties in examining the effect of ENSO on AR activity by solely using the atmospheric reanalysis. Note that other factors including Atlantic SST may also affect results of the composite analyses especially for the sustained ENSO years or ENSO transition years because of the limited sample size (see sections 3.2 and 5).

*2.2 Ensemble simulation in an AGCM*

To increase the signal-to-noise ratio in ENSO-related variability in mid-latitude AR activity, we use an ensemble model simulation output, similar to Kamae et al. (2017b, 2019). We use outputs of 10-member simulation (for 1958–2010) with an AGCM. The model in use is the Meteorological Research Institute Atmospheric General Circulation Model (MRI-AGCM) version 3.2 (Mizuta et al. 2012) at a horizontal resolution of TL319 (equivalent to 60-km mesh) with 64 vertical layers. Horizontal resolution of moisture transport data used for AR detection (section 2.3) is identical to JRA-55 (1.25° × 1.25°). The AGCM was driven by historical (1951–2010) variations in SST and sea ice (Hirahara et al. 2014) and radiative forcing agents (anthropogenic greenhouse gases, aerosols, ozone, and natural aerosols). More details of the experiments can be found in Mizuta et al. (2017) and Kamae et al. (2017b). This ensemble simulation output, called the Database for Probabilistic Description of Future Climate Change (d4PDF), is used to evaluate AR response to global SST variability and assess the effect of atmospheric internal variability (Kamae et al. 2017a, b). In this study, the 10-member ensemble mean and inter-member spread are considered as forced atmospheric response to SST and radiative forcing and internal atmospheric variability, respectively (Kamae et al. 2017a, b, Ueda et al. 2018; see section 3.2). Although d4PDF ensemble simulations facilitate the comparison of the two components (i.e., forced atmospheric response and internal variability), they only cover limited ENSO cases during 1958–2010, resulting in a difficulty in obtaining robust atmospheric responses to the sustained or transitioning ENSO forcing (see sections 3.2 and 5).

### *2.3 Detection of atmospheric rivers*

We detected ARs from 6-hourly atmospheric moisture transports in JRA-55 and d4PDF (sections 2.1, 2.2). Detection algorithm used in this study is based on Mundhenk et al. (2016) and slightly modified by Kamae et al. (2017b). In this algorithm, we use 6-hourly vertically integrated water vapor transport (IVT) between 300 and 1000 hPa levels calculated using specific humidity and horizontal wind at 1.25° × 1.25° spatial resolution. IVT is determined as:

$$\mathrm{IVT} = \sqrt{\left(\frac{1}{g}\int_{1000}^{300} qu\, dp\right)^2 + \left(\frac{1}{g}\int_{1000}^{300} qv\, dp\right)^2}\ , \qquad (1)$$

where $g$ is the acceleration due to gravity, $q$ is specific humidity, and $u$ and $v$ are zonal and meridional components of horizontal winds, respectively. Anomaly in IVT from its daily climatology is used to detect ARs so that the effect of climatological seasonal cycle of water vapor transport is excluded. Anomalous IVT larger than 140 kg $m^{-1}$ $s^{-1}$ is detected every 6 hours. Next, the identified water vapor transport bands with small area (< $7.8 \times 10^5$ $km^2$) or short length (< 1,500 km) or small length/width ratio (< 1.325) are removed. Note that long-term trends of obtained summertime AR frequency over the northwestern Pacific are small compared to the interannual variability (Kamae et al. 2017b). More details of the detection methods can be found in Mundhenk et al. (2016) and Kamae et al. (2017b).

*2.4 Linear baroclinic model*

We use a linear baroclinic model (LBM; Watanabe and Kimoto 2000) to diagnose linear atmospheric response to tropical diabatic heating related to seasonal transition of ENSO. This model is based on primitive equations linearized around the climatology of the observed atmospheric state based on NCEP/NCAR reanalysis (Kalnay et al. 1996). The model resolution is T42 (~2.8°) in the horizontal and 20 levels in the vertical. Details of experimental setups including background state and prescribed forcing are explained in section 4.2.

## 3. Seasonal ENSO transition and summertime AR activity over the North Pacific

### *3.1 AR frequency and atmospheric circulation over the North Pacific*

Seasonal-mean AR frequency in the nine groups are compared with the climatology for 1958–2010. Figure 2 shows composite anomalies of AR frequency and atmospheric circulation in association with wintertime and summertime ENSO phases in the simulations. Figure 3 shows the results for JRA-55. As shown in Kamae et al. (2017b), wintertime ENSO results in systematic anomaly of AR frequency over summertime East Asia. During post-El Niño summers, occurrence of ARs becomes more frequent over the western North Pacific compared to normal years, especially over the Pacific coasts of Japan (Figs. 2g–i, 3g–i). The relationship between wintertime ENSO and summertime East Asian AR frequency is generally explained as a result of anomalous WNPSH caused by the IPOC effect (Kamae et al. 2017b; see section 1). On the northwestern flank of WNPSH, anomalous southwesterly transports more water vapor from the South China Sea and the western North Pacific to East Asia during post-El Niño summers (Figs. 2g–i, 3g–i). Opposite is true for wintertime La Niña (i.e., relatively weak WNPSH and northeasterly anomaly on its northwestern flank during the summer) but with modest anomalies in sea level pressure (SLP) over the western North Pacific (Figs. 2a–c, 3a–c). In JRA-55, the circulation and AR anomalies are less systematic than d4PDF because of limited samples (Table 1).

In addition to the lagged influence, concurrent ENSO also modulates the North Pacific atmospheric circulation. During La Niña summers, easterly, westerly, and high-pressure anomalies are found over 20°–30°N, 40°–60°N, and 30°–50°N in the North Pacific, respectively (Figs. 2d, g, 3d, g). These are consistent with previous studies on the North Pacific SLP response to the summertime equatorial Pacific forcing (Lau et al. 2005; Paek et al. 2019; Kamae et al. 2019). The central-to-eastern equatorial Pacific cooling related to La Niña (Fig. 1a, d, g) suppresses convective heating aloft, favoring the negative phase of a tropics-to-midlatitudes atmospheric teleconnection called the Pacific/North America (PNA) pattern (Wallace and Gutzler 1981). Through this PNA teleconnection, positive SLP anomaly is consistently found over the North Pacific, indicating an intensification of the North Pacific High (NPH; Figs. 2d, g, 3d, g). The enhanced NPH results in an increase and decrease in AR frequency over 40°–60°N and 20°–40°N, respectively. Opposite anomalies are also found during the El Niño summers: weakened NPH, a decrease and an increase in AR frequency over 40°–60°N and 20°–40°N, respectively (Figs. 2f, i, 3f, i). Exceptions are the AR frequency and atmospheric circulation in a sustained La Niña year (Figs. 2a, 3a) and a La Niña-to-El Niño transition year (Figs. 2c, 3c) with small sample sizes (in 1971 and 1976, respectively).

*3.2 East-Asian AR activity*

The analyses in the previous section indicate that the seasonal transition of ENSO from winter to summer is a key for the prediction of summertime AR frequency over the North Pacific. Next, we focus on East Asia because this region often suffers from AR-caused heavy rainfall (Kamae et al. 2017c). Figure 4 shows East-Asian AR and circulation anomalies during post-El Niño summers in JRA-55 and d4PDF. To emphasize the effect of summertime ENSO, we compare the El Niño-to-La Niña transition years (Fig. 4a, c) and sustained El Niño years (Fig. 4b, d). During these years (i.e., both transition and sustained years), the subtropical western North Pacific experiences positive SLP anomalies and correspondingly increased AR frequency, as discussed in the previous section. Figure 5 shows AR frequency anomalies averaged over East Asia (110°–155°E; 25°–55°N, gray rectangle in Fig. 4). To assess year-to-year variability, we show AR frequency anomalies for individual transition and sustained years (see also Table 1). The East-Asian AR frequency (gray bars in Fig. 5) generally exhibit positive anomalies, consistent with Kamae et al. (2017b). No systematic differences are found between the transition years and sustained years (Fig. 5a, b).

In contrast, the regional patterns of the anomalies in SLP and AR frequency over East Asia are slightly different between the two (i.e., transition years and sustained years). The WNPSH is stronger and is more confined to the southern part during the sustained years

(Fig. 4b, d) than the transition years (Fig. 4a, c). The WNPSH anomaly in d4PDF simulation is only found over 10°–32°N during the sustained years (Fig. 4d), contrasting to that with a larger meridional extension (10°–40°N) in the transition years (Fig. 4c). Similar difference in meridional extent is also found in JRA-55 (10°–30°N in Fig. 4b and 10°–48°N in Fig. 4a). Note that the positions of the WNPSH anomalies during these years exhibit non-negligible difference between the JRA-55 and d4PDF, which will be discussed in section 5.

Regional patterns of AR frequency anomalies over East Asia are consistent with the WNPSH anomalies. The positive anomalies in AR frequency on the northwestern flank of the WNPSH is larger in the sustained years (Fig. 4b, d) than the transition years (Fig. 4a, c), consistent with the stronger WNPSH anomaly during the sustained years. Compared to the sustained years, the increase in AR frequency during the transition years are broader in space over northern part of East Asia (e.g. northeastern China, northern Japan, and around the Sea of Okhotsk; Fig. 4a, c), consistent with the meridional extent of the anomaly in the WNPSH. AR frequency averaged over northern East Asia (NEA; 110°–155°E; 40°–55°N, red dashed rectangle in Fig. 4) is shown in Fig. 5. The NEA region is defined as the northern boundary of the climatological AR occurrence over summertime East Asia (Fig. 3c in Kamae et al. 2017b). The seasonal-mean ARs over the NEA in the transition years are more frequent (especially in 2010) than the climatology (Figs. 4a, c, 5a, b). In contrast, AR frequency over the NEA is greatly reduced in the sustained years.

Generally, NEA AR frequency in JRA-55 exhibits larger year-to-year variations than that in the 10-member ensemble mean of d4PDF simulations (Fig. 5). This can be partly attributed to atmospheric internal variability (Kamae et al. 2017a, b). Error bars in Fig. 5b are generally large, indicating the great importance of atmospheric internal variability under the fixed radiative forcing and SST boundary conditions in the d4PDF simulations. Kamae et al. (2017a) showed that the relative importance of atmospheric internal variability compared to the forced atmospheric response to global SST perturbation is larger over the mid- and high-latitudes than the tropics (Fig. 10a, c of Kamae et al. 2017a). The d4PDF ensemble mean can be considered as a forced response to fixed boundary conditions because the effects of atmospheric internal variability cancel out each other (Kamae et al. 2017a, b, Ueda et al. 2018). However, the ensemble mean still exhibits large year-to-year variations under the similar ENSO transition, especially between 1973 and 2010 (Fig. 5b). The large variations suggest important effects of factors other than equatorial Pacific SST, for example, Indian Ocean SST, Atlantic SST, North Pacific SST, anthropogenic aerosol emissions, or volcanic eruptions. As an example, variability in the Atlantic SST possibly affects East Asian atmospheric circulation via changing tropical atmospheric circulation (e.g. Li et al. 2016; Kamae et al. 2017d) or mid-latitude circulation pattern (e.g. Liu et al. 2019). In addition, decadal-to-multidecadal variabilities may also affect AR activity discussed here because of their influence on mid-latitude atmospheric circulation (e.g. Newman et al. 2016; Kamae et al. 2017a; Tokinaga et al. 2019). Environmental factors responsible for the anomalies in AR activity in individual years will be further examined in future studies.

## 4. Possible importance of tropical heating

### *4.1 ENSO transition and tropical rainfall*

The results presented in the previous section indicate that: (1) the regional patterns of AR frequency over East Asia are different between El Niño transition years and sustained El Niño years; and (2) low-level atmospheric circulation is the key to the difference in AR frequency. The meridional patterns of AR frequency anomaly (broader positive anomaly in the transition years and south-positive north-negative pattern in the sustained years) found in JRA-55 (Fig. 4a, b) are largely reproduced in the model simulations (Fig. 4c, d). Note that the meridional positions of the AR frequency anomalies are significantly different between the simulations and observations (see section 5). In this section, possible importance of tropical SST forcing and associated diabatic heating to the differences in ARs and atmospheric circulation between transition and sustained years are examined.

Figure 6 shows summertime rainfall anomaly in the nine ENSO group years relative to the climatology in d4PDF simulations. Over the equatorial Pacific, rainfall anomaly is closely related to underlying SST anomalies (Fig. 1): the cool SST anomalies during the summertime La Niña years suppresses rainfall (Fig. 6a, d, g) and El Niño enhances rainfall over the equatorial Pacific (Fig. 6c, f, i). In addition, rainfall over the Maritime Continent is also strongly influenced by summertime ENSO. The rapid transition from El Niño to La Niña (Fig. 1g) favors easterly anomaly over the western-to-central tropical Pacific and anomalous convergence over the Maritime Continent in the lower troposphere (Figs. 2g, 3g), resulting in a great increase in rainfall (Fig. 6g). This is consistently found in satellite observations with a limited sample size (Supplement 1) and in line with previous studies showing that the zonal SST gradient over the Indian and Pacific Oceans are of great importance to the rainfall over the tropical western North Pacific (e.g. Ohba and Ueda 2006; Wu et al. 2010; Ueda et al. 2015). During sustained El Niño years, tropical rainfall anomaly exhibits a distinct pattern compared to the transition years. The zonal gradient in rainfall anomaly over the Maritime Continent and the central equatorial Pacific during the sustained years (Fig. 6i, Supplement 1) is opposite to that in the transition years, consistent with the difference in zonal gradient of underlying SST (Fig. 1i). We assume that the summertime SST forcing and associated condensation heating over the Maritime Continent and the equatorial Pacific are also important for the circulation and AR frequency over the western North Pacific and East Asia in addition to the preceding-winter ENSO forcing (Kamae et al. 2017b). To confirm this hypothesis, we conducted numerical simulations using the LBM (section 2.4).

*4.2 Atmospheric response to tropical forcing*

In this subsection, we explore the possible importance of tropical diabatic heating to the circulation and AR frequency anomaly examined in the previous sections. We use the LBM to examine a linear atmospheric response to the anomalous atmospheric heating in the El Niño transition years relative to the climatology. As shown in the previous section, tropical rainfall exhibits a zonal pair of positive and negative anomalies over the Maritime Continent and western-to-central equatorial Pacific, distinct from what occurs in the sustained years (Fig. 6g, i, Supplement 1). The anomalous convective heating/cooling are prescribed in the LBM. Background atmospheric state is a JJA climatology obtained from the NCEP/NCAR reanalysis (section 2.4). The response at day 20 when the model reaches a quasi-steady state is analyzed.

Figure 7 shows the steady atmospheric response to the tropical diabatic heating. We conducted two experiments: first, the model was forced by a pair of diabatic cooling and heating, which have a deep vertical structure with its rate peaking at 454 hPa (–1 K day$^{-1}$ and 1 K day$^{-1}$), centered at 180°E, 0°N and 120°E, 0°N, respectively; second, the model was forced solely by the equatorial Pacific cooling. The vertical structure is consistent with the climatological diabatic heating over these regions (Yanai and Tomita 1998). We can examine effects of the two (i.e., the Maritime Continent heating and the Pacific cooling) by comparing the two experiments. The equatorial heating/cooling pair favor a positive WNPSH anomaly (Fig. 7a), largely consistent with the observed and simulated WNPSH anomaly in the El Niño-to-La Niña transition years (Fig. 4a, c). The equatorial heating over the Maritime Continent favors eastward propagating Kelvin waves over the western-to-central equatorial Pacific, similar to the atmospheric response to the Indian Ocean warming (Xie et al. 2009; see section 1). The intensified northeasterly trades over the central tropical Pacific contribute to the enhancement of the WNPSH.

When only the equatorial Pacific cooling is prescribed (Fig. 7b), a pair of zonally-elongated low-level anticyclonic circulation anomalies is favored over the western tropical Pacific to the north and south of the equator. This pair of anticyclones can be simply understood as a Rossby response to the equatorial cooling (Gill 1980). The WNPSH anomaly found in this experiment is consistent with that observed in years with cool SST anomaly over the central Pacific (Wang et al. 2013; Paek et al. 2019). However, the positive response in SLP found here is confined to a narrower meridional extent (0°–30°N) compared to the heating/cooling pair experiment (Fig. 7a). The northern edge of the WNPSH anomaly (Fig. 7b) is not consistent with those found in Figs. 4a (48°N) and 4c (40°N), suggesting that the Pacific cooling is not sufficient to explain the circulation and AR frequency anomalies over the NEA found in the El Niño transition years (Fig. 4a, c). Instead, both the heating over the Maritime Continent and the cooling over the Pacific Ocean are important, as demonstrated earlier (Fig. 7a).

## 5. Summary and discussion

We examined interannual variability in East Asian AR frequency and associated summertime atmospheric circulation with a focus on influence of seasonal transition of ENSO from preceding winter to summer. Using JRA-55 reanalysis and d4PDF ensemble simulations, we showed that rapid transitions from wintertime El Niño to summertime La

Niña increase the occurrence of ARs over NEA but do not significantly change total occurrence over East Asia compared to sustained El Niño years. In addition to the wintertime El Niño forcing, summertime cool SST over the central-to-eastern Pacific related to La Niña results in strong zonal SST gradient and associated heating gradient in the tropical atmosphere. Linear steady response of the atmosphere to the zonal heating gradient is characterized by a meridionally-elongated anticyclone over the subtropical western North Pacific, consistent with the atmospheric circulation anomaly found in the composite analysis. The combination of the WNPSH anomaly rooted from the preceding-winter El Niño and the meridionally-elongated anticyclonic anomaly favored by the summertime La Niña is effective in increasing AR frequency over the NEA, suggesting the importance of a reliable prediction of ENSO seasonal transitions for the prediction of AR-related disaster risk over the NEA.

The latitudinal positions of the WNPSH anomaly in JRA-55 and d4PDF are significantly different, resulting in difficulties in an accurate prediction of regional AR-related disaster risk. One possible factor for the observation-model inconsistency is the difference in sample size. The composite analyses in this study are based on limited samples, for example cases of sustained La Niña year (1971), sustained El Niño years (1983, 1987), La Niña-to-El Niño transition year (1976) and El Niño-to-La Niña transition years (1973, 2010). Because of the impact of atmospheric internal variability, it is difficult to detect SST-forced signals over the mid-latitudes, especially from the atmospheric reanalysis (Kamae et al.

2017a). Even in the ensemble simulations, the sample size still prevents from obtaining robust atmospheric responses to the ENSO forcing (Fig. 5). To reduce the effects other than the ENSO-related SST (section 3.2), larger samples obtained from longer integrations using coupled atmosphere-ocean general circulation models (e.g. Kay et al. 2016) may be more favorable.

Another important factor for the observation-model inconsistency is the inherent deficiencies in fixed-SST simulations. In the AGCM simulations, prescribed SST boundary condition may result in unrealistic atmospheric responses. Wang et al. (2005) showed that the atmosphere-ocean coupling over the western North Pacific found in the observations is not reproduced in fixed-SST simulations by an AGCM. Zhou et al. (2009) further pointed out that AGCMs have limited skills in reproducing interannual variation of atmospheric circulation over the extratropical East Asia. The AGCM-based results shown in the present study are consistent with reanalysis in terms of northward expansion of the WNPSH and NEA AR frequency, but other regional features are inconsistent. We plan to conduct further tests using high-resolution atmosphere-ocean coupled model simulations (e.g., Haarsma et al. 2018) to better understand of the influence of ENSO transition on East-Asian AR activity.

**Supplement**

Supplement 1 provides satellite observations of summertime rainfall anomaly compared to climatology.

## Acknowledgments

This work was supported by JSPS KAKENHI Grant Numbers 19H05704, 17K14388 and 17K01223, and the Integrated Research Program for Advancing Climate Models (TOUGOU program) from the Ministry of Education, Culture, Sports, Science and Technology (MEXT), Japan. The Earth Simulator was used for the d4PDF ensemble simulation as “Strategic Project with Special Support” of JAMSTEC. The d4PDF dataset is available via DIAS website (http://search.diasjp.net/en/dataset/d4PDF_GCM). We are grateful to Dr. T. Sato and two anonymous reviewers for their constructive comments.

## References

American Meteorological Society, 2019: Atmospheric river. Glossary of Meteorology. Amer. Meteor. Soc. [Available at http://glossary.ametsoc.org/wiki/Atmospheric_river.]

Espinoza, V., D. E. Waliser, B. Guan, D. A. Lavers, and F. M. Ralph, 2018: Global analysis of climate change projection effects on atmospheric rivers. *Geophys. Res. Lett.*, **45**, 4299–4308.

Gill, A. E., 1980: Some simple solutions for heat-induced tropical circulation. *Quart. J. Royal Meteor. Soc.*, **106**, 447–462.

Gimeno, L., R. Nieto, M. Vázquez, and D. A. Lavers, 2014: Atmospheric rivers: A mini-review. *Front. Earth Sci.*, **2**, 2.1–2.6.

Gimeno, L., F. Dominguez, R. Nieto, R. Trigo, A. Drumond, C. J. C. Reason, A. S. Taschetto, A. M. Ramos, R. Kumar, and J. Marengo, 2016: Major mechanisms of atmospheric moisture transport and their role in extreme precipitation events. *Ann. Rev. Environ. Res.*, **41**, 117–141.

Guan, B., and D. E. Waliser, 2015: Detection of atmospheric rivers: Evaluation and application of an algorithm for global studies. *J. Geophys. Res.*, **120**, 12514–12535.

Guan, B., and D. E. Waliser, 2019: Tracking atmospheric rivers globally: Spatial distributions and temporal evolution of life cycle characteristics. *J. Geophys. Res.*, doi: 10.1029/2019JD031205.

Haarsma, R. J., et al, 2018: High resolution model intercomparison project (HighResMIP v1.0) for CMIP6. *Geosci. Model Dev.*, **9**, 4185–4208.

Hirahara, S., M. Ishii, and Y. Fukuda, 2014: Centennial-scale sea surface temperature analysis and its uncertainty. *J. Climate*, **27**, 57–75.

Hirota, N., Y. N. Takayabu, M. Kato, and S. Arakane, 2016: Roles of an atmospheric river and a cutoff low in the extreme precipitation event in Hiroshima on 19 August 2014. *Mon. Wea. Rev.*, **144**, 1145–1160.

Kalnay, E., M. Kanamitsu, R. Kistler, et al., 1996: The NCEP/NCAR 40-year reanalysis project. *Bull. Amer. Meteor. Soc.*, **77**, 437–470.

Kamae, Y., H. Shiogama, Y. Imada, M. Mori, O. Arakawa, R. Mizuta, K. Yoshida, C. Takahashi, M. Arai, M. Ishii, M. Watanabe, M. Kimoto, S.-P. Xie, and H. Ueda, 2017a:

Forced response and internal variability of summer climate over western North America. *Climate Dyn.*, **49**, 403-417.

Kamae, Y., W. Mei, S.-P. Xie, M. Naoi, and H. Ueda, 2017b: Atmospheric rivers over the Northwestern Pacific: Climatology and interannual variability. *J. Climate*, **30**, 5605–5619.

Kamae, Y., W. Mei, and S.-P. Xie, 2017c: Climatological relationship between warm season atmospheric rivers and heavy rainfall over East Asia. *J. Meteor. Soc. Japan*, **95**, 411–431.

Kamae, Y., X. Li, S.-P. Xie, and H. Ueda, 2017d: Atlantic effects on recent decadal trends in global monsoon. *Climate Dyn.*, **49**, 3443–3455.

Kamae, Y., W. Mei, and S.-P. Xie, 2019: Ocean warming pattern effects on future changes in East Asian atmospheric rivers. *Env. Res. Lett.*, **14**, 054019. doi:10.1088/1748-9326/ab128a.

Kay, J. E., C. Deser, A. Phillips, et al., 2015: The Community Earth System Model (CESM) large ensemble project: A community resource for studying climate change in the presence of internal climate variability. *Bull. Amer. Meteor. Soc.*, **96**, 1333–1349.

Kobayashi, S., Y. Ota, Y. Harada, A. Ebita, M. Moriya, H. Onda, K. Onogi, H. Kamahori, C. Kobayashi, H. Endo, K. Miyaoka, and K. Takahashi, 2015: The JRA-55 Reanalysis: General specifications and basic characteristics. *J. Meteor. Soc. Japan*, **93**, 5–48.

Lau, N. C., A. Leetmaa, M. J. Nath, and H. L. Wang, 2005: Influences of ENSO-induced Indo-Western Pacific SST anomalies on extratropical atmospheric variability during the boreal summer. *J. Climate*, **18**, 2922–2942.

Li, X., S.-P. Xie, S. T. Gille, and C. Yoo, 2016: Atlantic-induced pan-tropical climate change over the past three decades. *Nature Climate Change*, **6**, 275–279.

Liu, B., C. Zhu, J. Su, S. Ma, and K. Xu, 2019: Record-breaking northward shift of the western North Pacific Subtropical High in July 2018. *J. Meteor. Soc. Japan*, **97**, 913–925.

Mizuta, R., H. Yoshimura, H. Murakami, M. Matsueda, H. Endo, T. Ose, K. Kamiguchi, M. Hosaka, M. Sugi, S. Yukimoto, S. Kusunoki, and A. Kitoh, 2012: Climate simulations using MRI-AGCM3.2 with 20-km grid. *J. Meteor. Soc. Japan*, **90A**, 233–258.

Mizuta, R., A. Murata, M. Ishii, et al., 2017: Over 5000 years of emsemble future climate simulations by 60km global and 20km regional atmospheric models. *Bull. Amer. Meteor. Soc.*, **98**, 1383–1398.

Mundhenk, B. D., E. A. Barnes, and E. D. Maloney, 2016: All-season climatology and variability of atmospheric river frequencies over the North Pacific. *J. Climate*, **29**, 4885–4903.

Newman, M., M. A. Alexander, T. R. Ault, et al., 2016: The Pacific decadal oscillation, revisited. *J. Climate*, **29**, 4399–4427.

Ohba, M., and H. Ueda, 2006: A role of zonal gradient of SST between the Indian Ocean and the western Pacific in localized convection around the Philippines. *SOLA*, **2**, 176–179.

Paek, H., J. Y. Yu, F. Zheng, and M. M. Lu, 2019: Impacts of ENSO diversity on the western

Pacific and North Pacific subtropical highs during boreal summer. *Climate Dyn.*, **52**, 7153–7172.

Ralph, F. M., P. J. Neiman, G. N. Kiladis, K. Weickmann, and D. W. Reynolds, 2011: A multiscale observational case study of a Pacific atmospheric river exhibiting tropical/extratropical connections and a mesoscale frontal wave. *Mon. Wea. Rev.*, **139**, 1169–1189.

Shields, C. A., J. J. Rutz, L. Y. Leung, et al. 2018: Atmospheric river tracking method intercomparison project (ARTMIP): project goals and experimental design. *Geosci. Model Dev.*, **11**, 2455–2474.

Shimpo, A., K. Takemura, S. Wakamatsu, et al. 2019: Primary factors behind the heavy rain event of July 2018 and the subsequent heat wave in Japan. *SOLA*, **15A**, 13–18.

Stein, K., N. Schneider, A. Timmermann, and F.-F. Jin, 2010: Seasonal synchronization of ENSO events in a linear stochastic model. *J. Climate*, **23**, 5629–5643.

Takemura, K., S. Wakamatsu, H. Togawa, A. Shimpo, C. Kobayashi, S. Maeda, and H. Nakamura, 2019: Extreme moisture flux convergence over western Japan during the heavy rain event of July 2018. *SOLA*, doi:10.2151/sola.15A-009.

Tokinaga, H., S.-P. Xie, and H. Mukougawa, 2017: Early 20th-century Arctic warming intensified by Pacific and Atlantic multidecadal variability. *PNAS*, **114**, 6227–6232.

Tsuguchi, H., N. Seino, H. Kawase, Y. Imada, T. Nakaegawa and I. Takayabu, 2019: Meteorological overview and mesoscale characteristics of the heavy rain event of July

2018 in Japan. *Landslides*, **16**, 363–371.

Tsuji, H., and Y. N. Takayabu 2019: Precipitation enhancement via the interplay between atmospheric rivers and cutoff lows. *Mon. Wea. Rev.*, **149**, 2451–2466.

Ueda, H., Y. Kamae, M. Hayasaki, A. Kitoh, S. Watanabe, Y. Miki, and A. Kumai, 2015: Combined effects of recent Pacific cooling and Indian Ocean warming on the Asian monsoon. *Nature Comm.*, **6**, 8854, doi:10.1038/ncomms9854.

Ueda, H., K. Miwa, and Y. Kamae, 2018: Seasonal modulation of tropical cyclone occurrence associated with coherent Indo-Pacific variability during decaying phase of El Niño. *J. Meteor. Soc. Japan*, **96**, 381–390.

Waliser, D., and B. Guan, 2017: Extreme winds and precipitation during landfall of atmospheric rivers. *Nature Geosci.*, **10**, 179–183.

Wallace, J. M., and D. S. Gutzler, 1981: Teleconnections in the geopotential height field during the Northern Hemisphere winter. *Mon. Wea. Rev.*, **109**, 784–812.

Wang, B., R. Wu, and X. Fu, 2000: Pacific-east Asian teleconnection: How does ENSO affect east Asian climate? *J. Climate*, **13**, 1517–1536.

Wang, B., Q. H. Ding, X. H. Fu, I.-S. Kang, K. Jin, J. Shukla, and F. Doblas-Reyes, 2005: Fundamental challenge in simulation and prediction of summer monsoon rainfall. *Geophys. Res. Lett.*, **32**, L15711, doi:10.1029/2005GL022734.

Wang, B., B. Xiang, and J. -Y. Lee, 2013: Subtropical high predictability establishes a promising way of monsoon and tropical storm predictions. *PNAS*, **110**, 2718–2722.

Watanabe, M., and M. Kimoto, 2000: Atmosphere–ocean thermal coupling in the North Atlantic: a positive feedback. *Quart. J. Royal Meteor. Soc.*, **126**, 3343–3369.

Wu, B., T. Li, and T. J. Zhou, 2010: Relative contributions of the Indian Ocean and local SST anomalies to the maintenance of the western North Pacific anomalous anticyclone during the El Niño decaying summer. *J. Climate*, **23**, 2974–2986.

Xie, S.-P., Hu, K., J. Hafner, H. Tokinaga, Y. Du, G. Huang, and T. Sampe, 2009: Indian Ocean capacitor effect on Indo-western Pacific climate during the summer following El Niño. *J. Climate*, **22**, 730–747.

Xie, S.-P., Y. Kosaka, Y. Du, K. Hu, J.S. Chowdary, and G. Huang, 2016: Indo-western Pacific Ocean capacitor and coherent climate anomalies in post-ENSO summer: A review. *Adv. Atmos. Sci.*, **33**, 411–432.

Yanai, M., and T. Tomita, 1998: Seasonal and interannual variability of atmospheric heat sources and moisture sinks as determined from NCEP–NCAR reanalysis. *J. Climate*, **11**, 463–482.

Zhou, T., B. Wu, and B. Wang, 2009: How well do atmospheric general circulation models capture the leading modes of the interannual variability of the Asian–Australian monsoon? *J. Climate*, **22**, 1159–1173.

## List of Tables

Table 1. List of years used for composite analyses. Row and column indicate El Niño,

neutral, and La Niña years for 1958–2010 during preceding December-to-February (DJF) and June-to-August (JJA), respectively.

## List of Figures

Fig. 1 Composited sea surface temperature (SST; K) anomaly during June-to-August (JJA) compared to the climatology for 1958–2010 in (a) years with preceding-winter La Niña and concurrent La Niña (La Niña to La Niña; indicated as “LtoL” in the subplot title; Table 1), (b) decaying La Niña (La Niña to Neutral) years, (c) years with a transition from La Niña to El Niño, (d) developing La Niña (Neutral to La Niña) years, (e) neutral years, (f) developing El Niño (Neutral to El Niño) years, (g) years with a transition from El Niño to La Niña, (h) decaying El Niño (El Niño to Neutral) years, and (i) sustained El Niño (El Niño to El Niño) years. Stipples indicate regions with anomalies statistically significant at 0.05 level.

Fig. 2 As in Fig. 1, but for the occurrence frequency of atmospheric rivers (ARs; shading; %), sea level pressure (SLP; contour; hPa), and horizontal wind at 850 hPa level (vector; m $s^{-1}$) simulated in d4PDF. Solid and dashed contours indicate positive (0.4, 1, 2, 4 and 6 hPa) and negative (–6, –4, –2, –1 and –0.4 hPa) SLP anomalies, respectively. Stipples indicate regions with anomalies statistically significant at 0.05 level.

Fig. 3 As in Fig. 2, but for JRA-55.

Fig. 4 Reprint of (a) Fig. 3g, (b) 3i, (c) 2g and (d) 2i, but for East Asia. Gray solid and red dashed rectangles indicate regions of East Asia (110°–155°E; 25°–55°N) and northern

East Asia (NEA; 110°–155°E; 40°–55°N) examined in Fig. 5, respectively.

Fig. 5. Anomalies in AR occurrence frequency (%) averaged over East Asia (gray rectangle in Fig. 4) and the NEA (red dashed rectangle in Fig. 4) for El Niño-to-La Niña transition years (1973 and 2010; blue) and sustained El Niño years (1983 and 1987; orange) in (a) JRA-55 and (b) d4PDF. Gray bars and colored (blue or orange) bars show East Asian and NEA ARs, respectively. Error bars in (b) indicate 95% statistically significant confidence intervals.

Fig. 6. As in Fig. 2, but for rainfall (mm day$^{-1}$).

Fig. 7. Atmospheric response to tropical diabatic heating simulated with Linear Baroclinic Model. (a) Atmospheric response to the Maritime Continent heating and the Pacific cooling found in El Niño-to-La Niña transition years (Fig. 4g). (b) Atmospheric response to the Pacific cooling. Shading indicate stream function at 850 hPa ($10^6$ m$^2$ s$^{-1}$). Dashed and solid contours indicate prescribed cooling (–0.6 and –0.2 K day$^{-1}$) and heating (0.2 and 0.6 K day$^{-1}$) at 454 hPa, respectively.

Table 1. List of years used for composite analyses. Row and column indicate El Niño, neutral, and La Niña years for 1958–2010 during preceding December-to-February (DJF) and June-to-August (JJA), respectively.

| | | JJA(0) | | |
|---|---|---|---|---|
| | | La Niña | Neutral | El Niño |
| DJF(–1) | La Niña | 1971 | 1968, 1974, 1989, 2000, 2008 | 1976 |
| | Neutral | 1960, 1961, 1964, 1967, 1970, 1975, 1978, 1984, 1985, 1988, 1999 | 1959, 1962, 1977, 1979, 1980, 1981, 1986, 1990, 1994, 1995, 1996, 2001, 2003, 2004, 2005, 2006, 2007 | 1963, 1965, 1969, 1972, 1982, 1991, 1993, 1997, 2002, 2009 |
| | El Niño | 1973, 2010 | 1958, 1966, 1992, 1998 | 1983, 1987 |

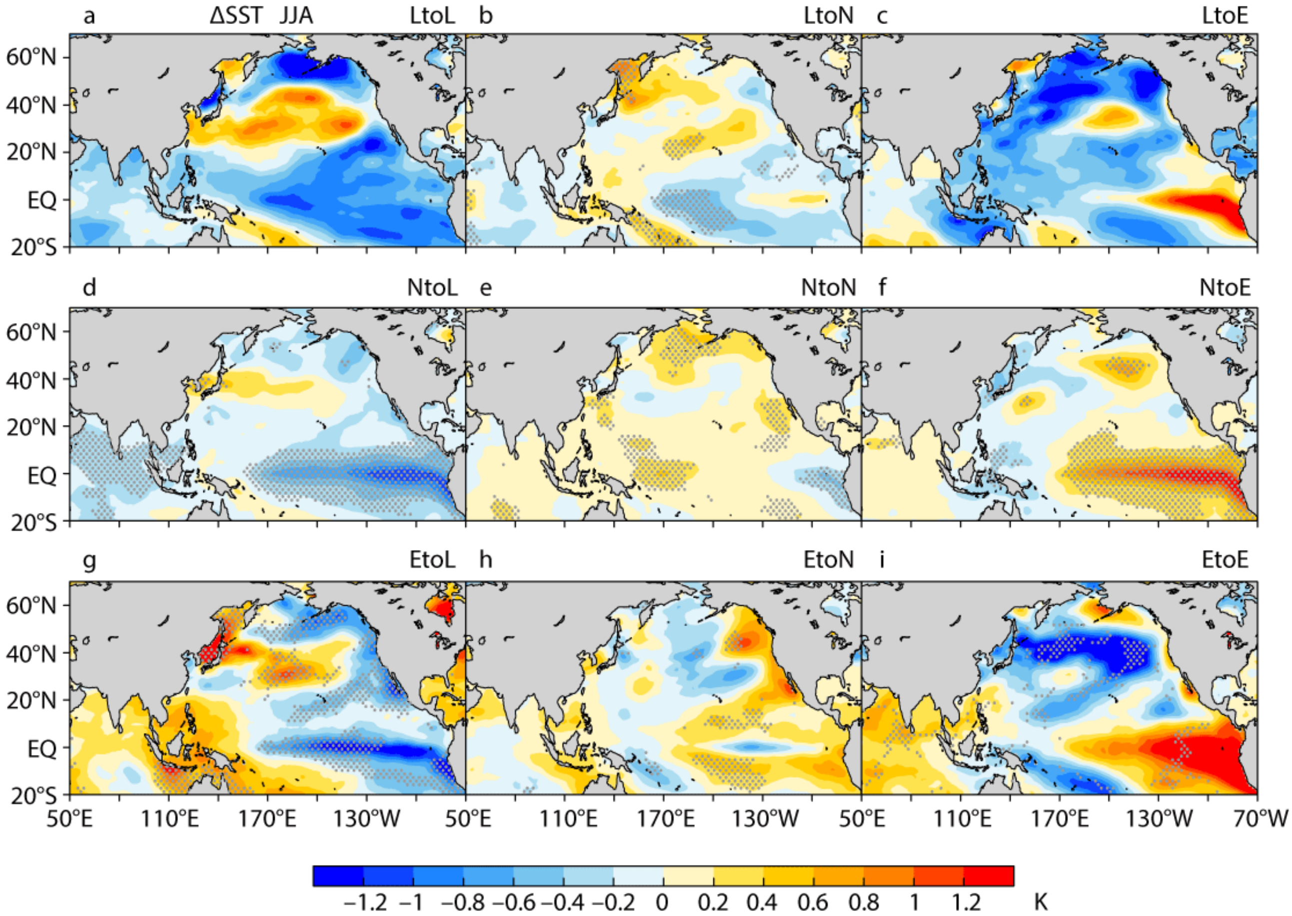


Fig. 1 Composited sea surface temperature (SST; K) anomaly during June-to-August (JJA) compared to the climatology for 1958–2010 in (a) years with preceding-winter La Niña and concurrent La Niña (La Niña to La Niña; indicated as “LtoL” in the subplot title; Table 1), (b) decaying La Niña (La Niña to Neutral) years, (c) years with a transition from La Niña to El Niño, (d) developing La Niña (Neutral to La Niña) years, (e) neutral years, (f) developing El Niño (Neutral to El Niño) years, (g) years with a transition from El Niño to La Niña, (h) decaying El Niño (El Niño to Neutral) years, and (i) sustained El Niño (El Niño to El Niño) years. Stipples indicate regions with anomalies statistically significant at 0.05 level.

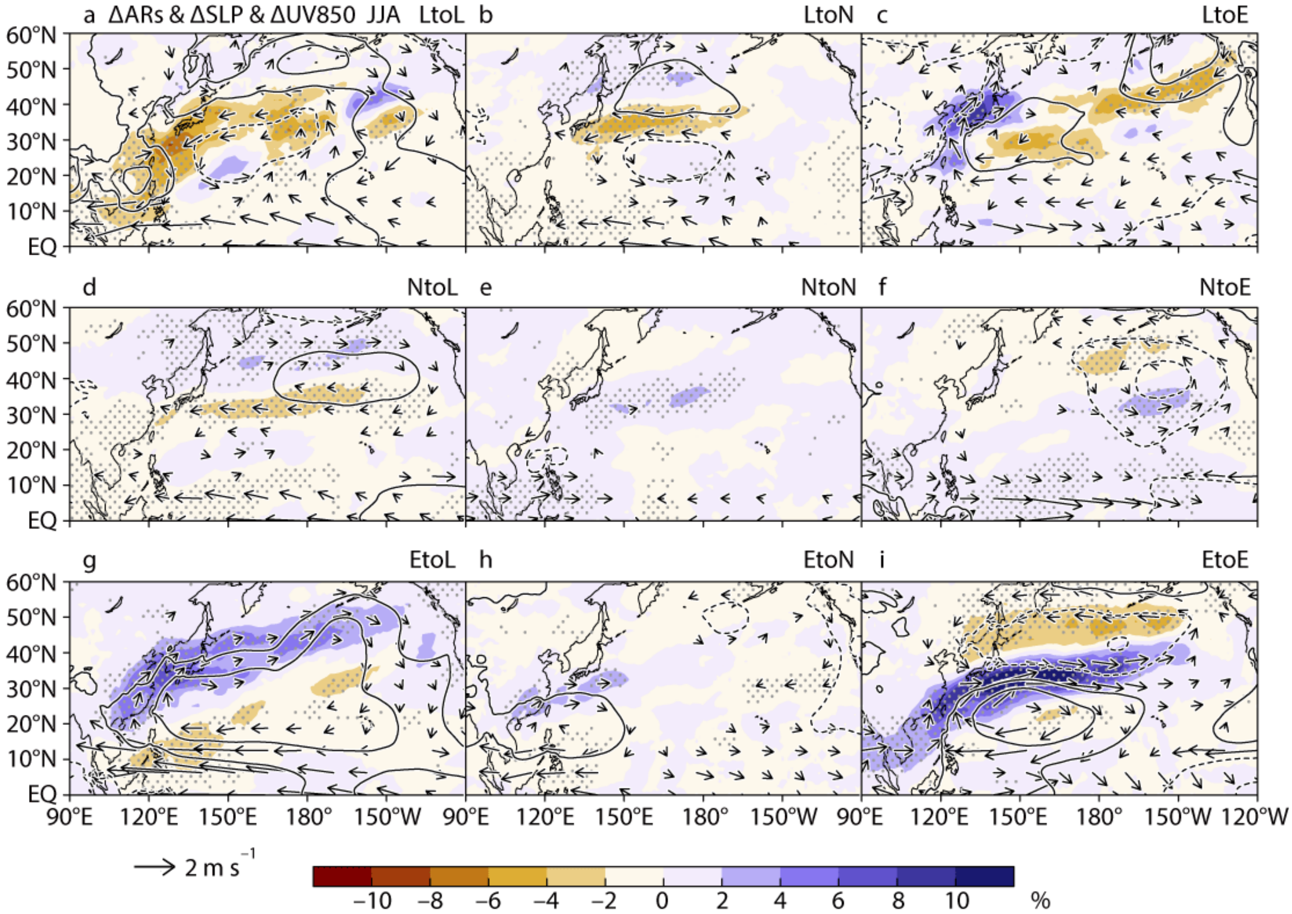


Fig. 2 As in Fig. 1, but for the occurrence frequency of atmospheric rivers (ARs; shading; %), sea level pressure (SLP; contour; hPa), and horizontal wind at 850 hPa level (vector; m $s^{-1}$) simulated in d4PDF. Solid and dashed contours indicate positive (0.4, 1, 2, 4 and 6 hPa) and negative (–6, –4, –2, –1 and –0.4 hPa) SLP anomalies, respectively. Stipples indicate regions with anomalies statistically significant at 0.05 level.

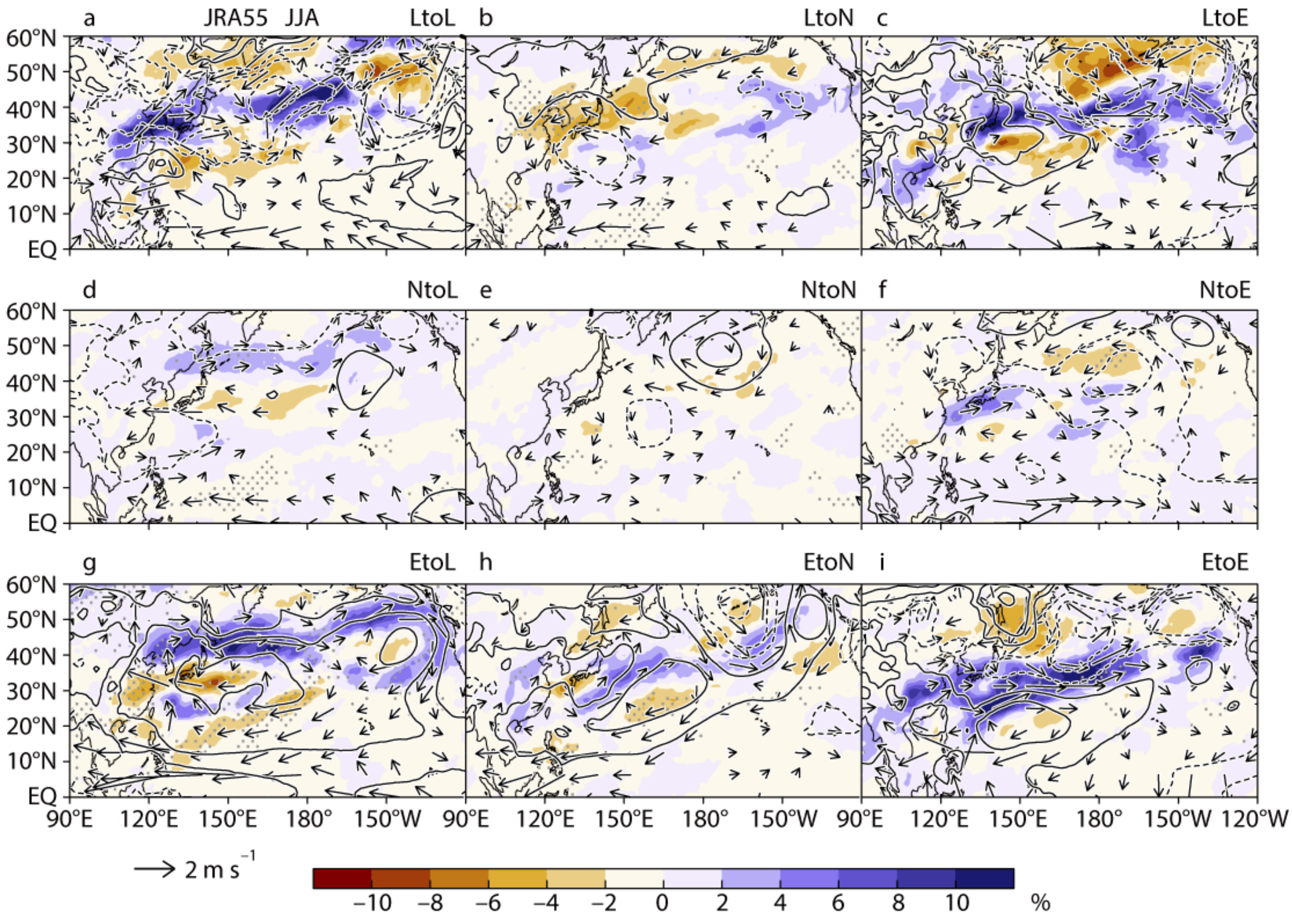


Fig. 3 As in Fig. 2, but for JRA-55.

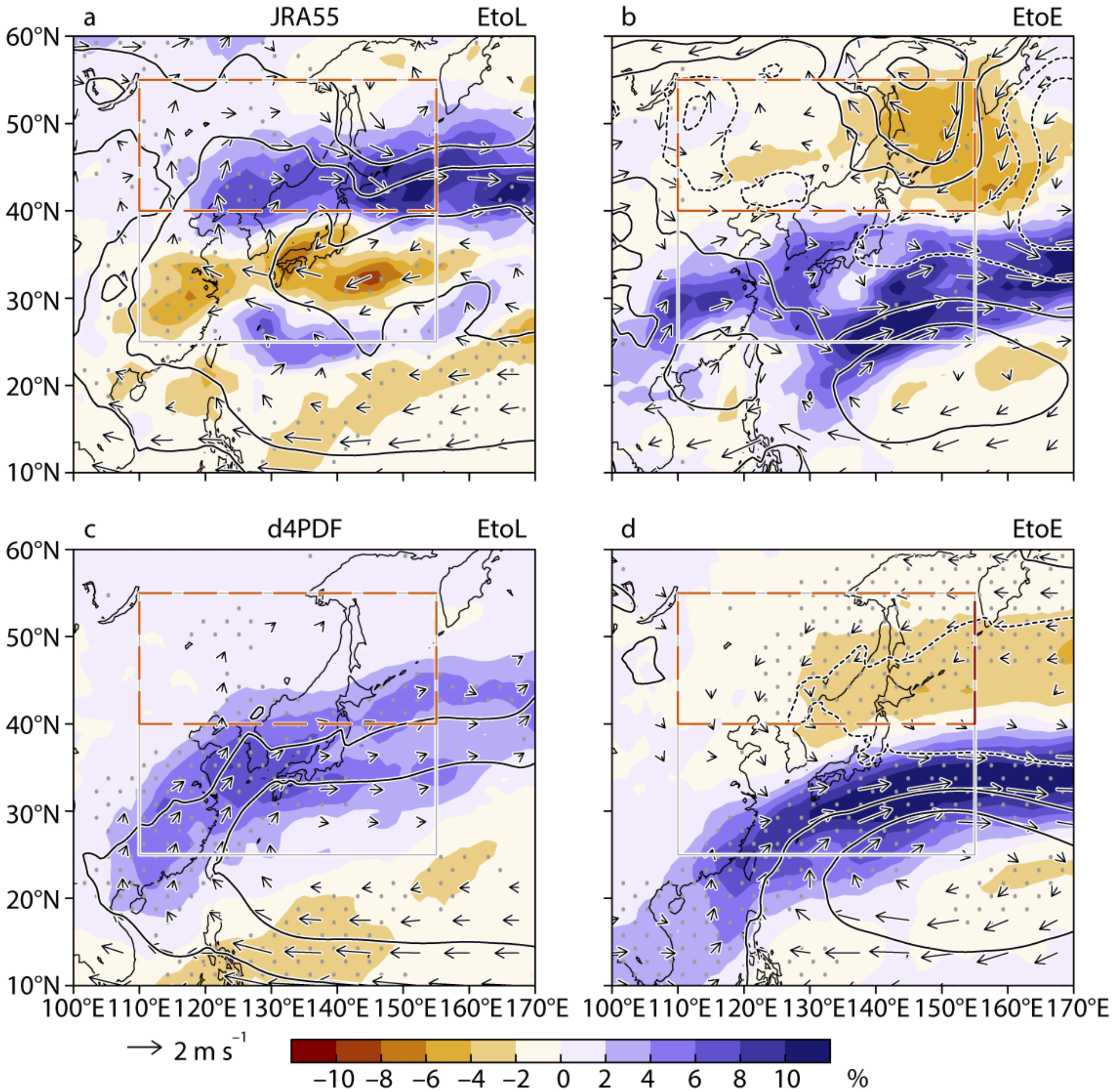


Fig. 4 Reprint of (a) Fig. 3g, (b) 3i, (c) 2g and (d) 2i, but for East Asia. Gray solid and red dashed rectangles indicate regions of East Asia (110°–155°E; 25°–55°N) and northern East Asia (NEA; 110°–155°E; 40°–55°N) examined in Fig. 5, respectively.

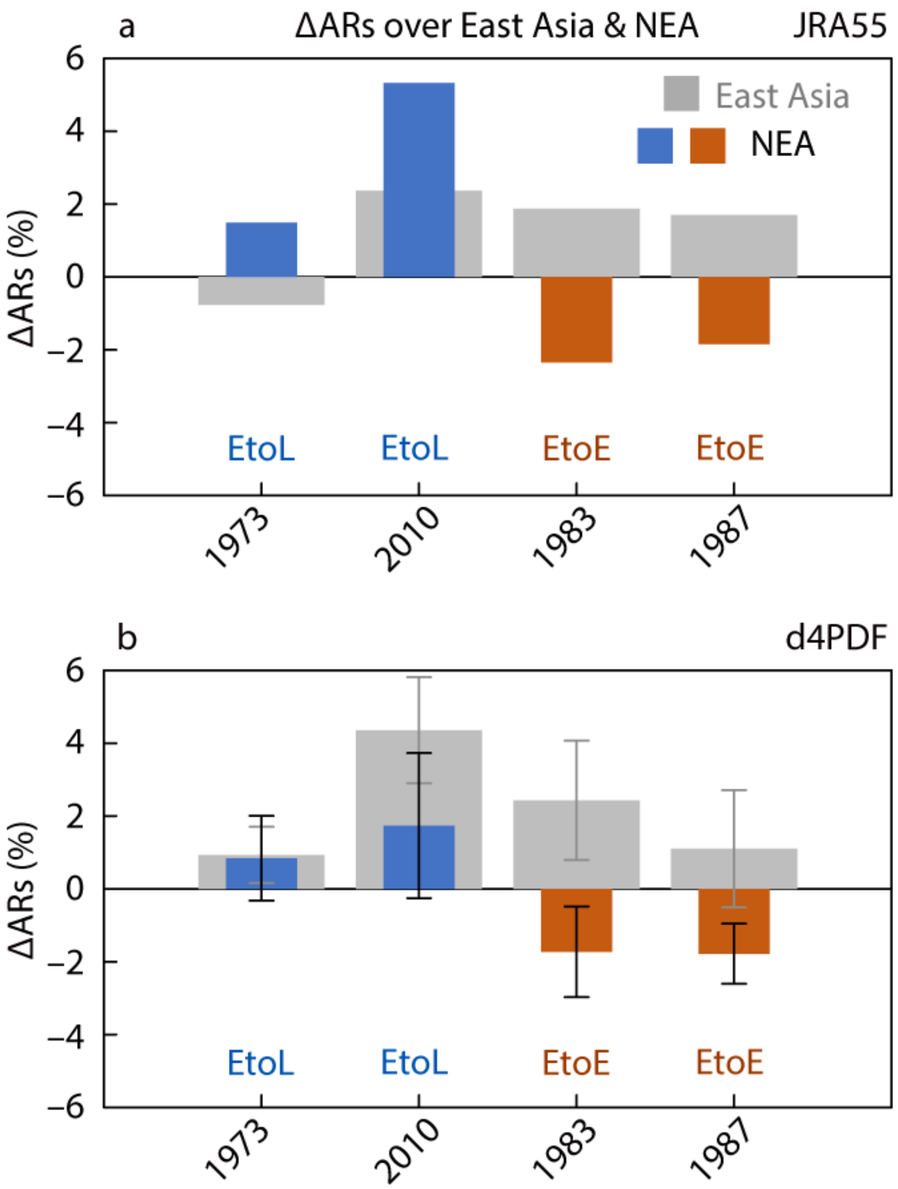


Fig. 5. Anomalies in AR occurrence frequency (%) averaged over East Asia (gray rectangle in Fig. 4) and the NEA (red dashed rectangle in Fig. 4) for El Niño-to-La Niña transition years (1973 and 2010; blue) and sustained El Niño years (1983 and 1987; orange) in (a) JRA-55 and (b) d4PDF. Gray bars and colored (blue or orange) bars show East Asian and NEA ARs, respectively. Error bars in (b) indicate 95% statistically significant confidence intervals.

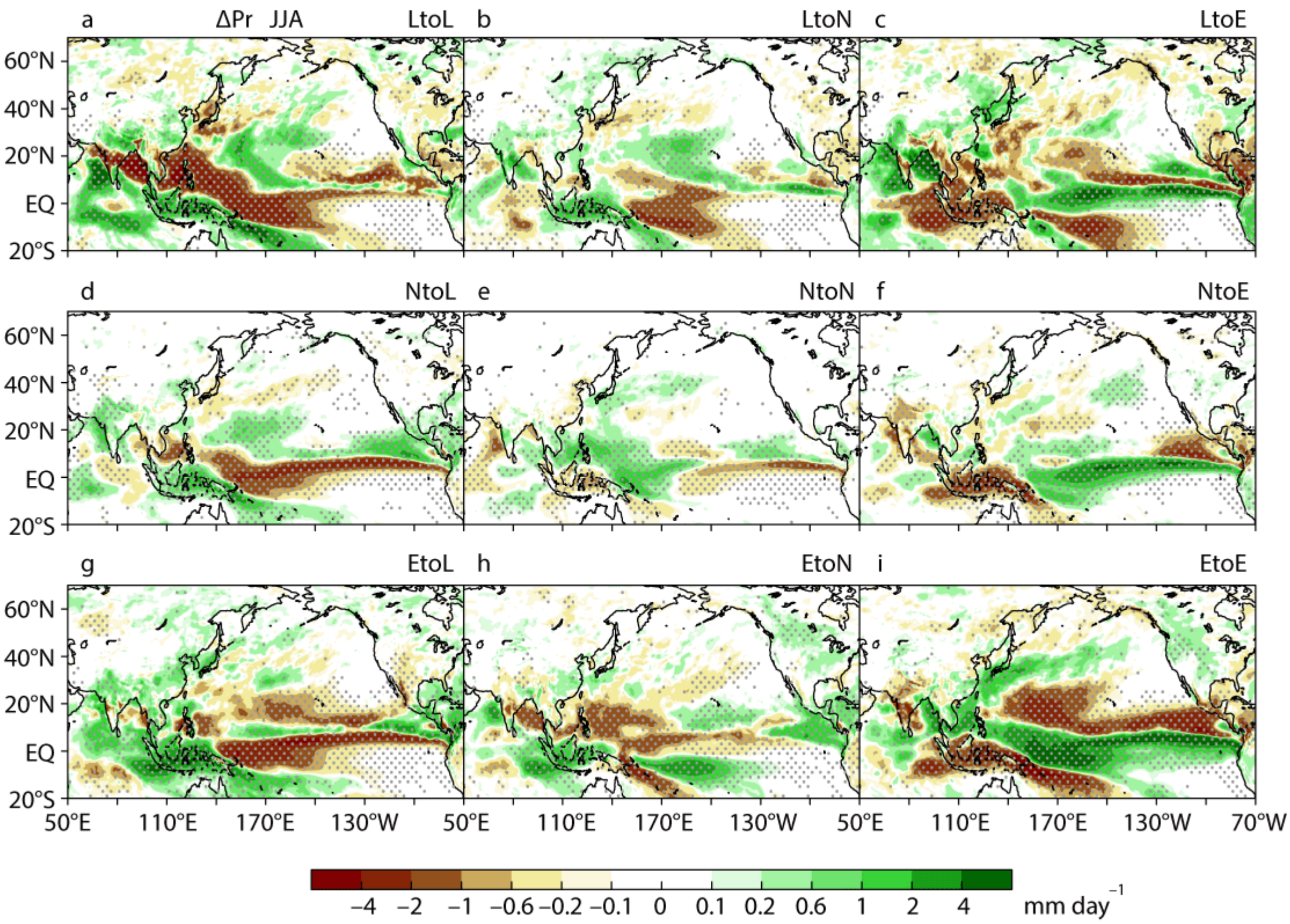


Fig. 6. As in Fig. 2, but for rainfall (mm day$^{-1}$).

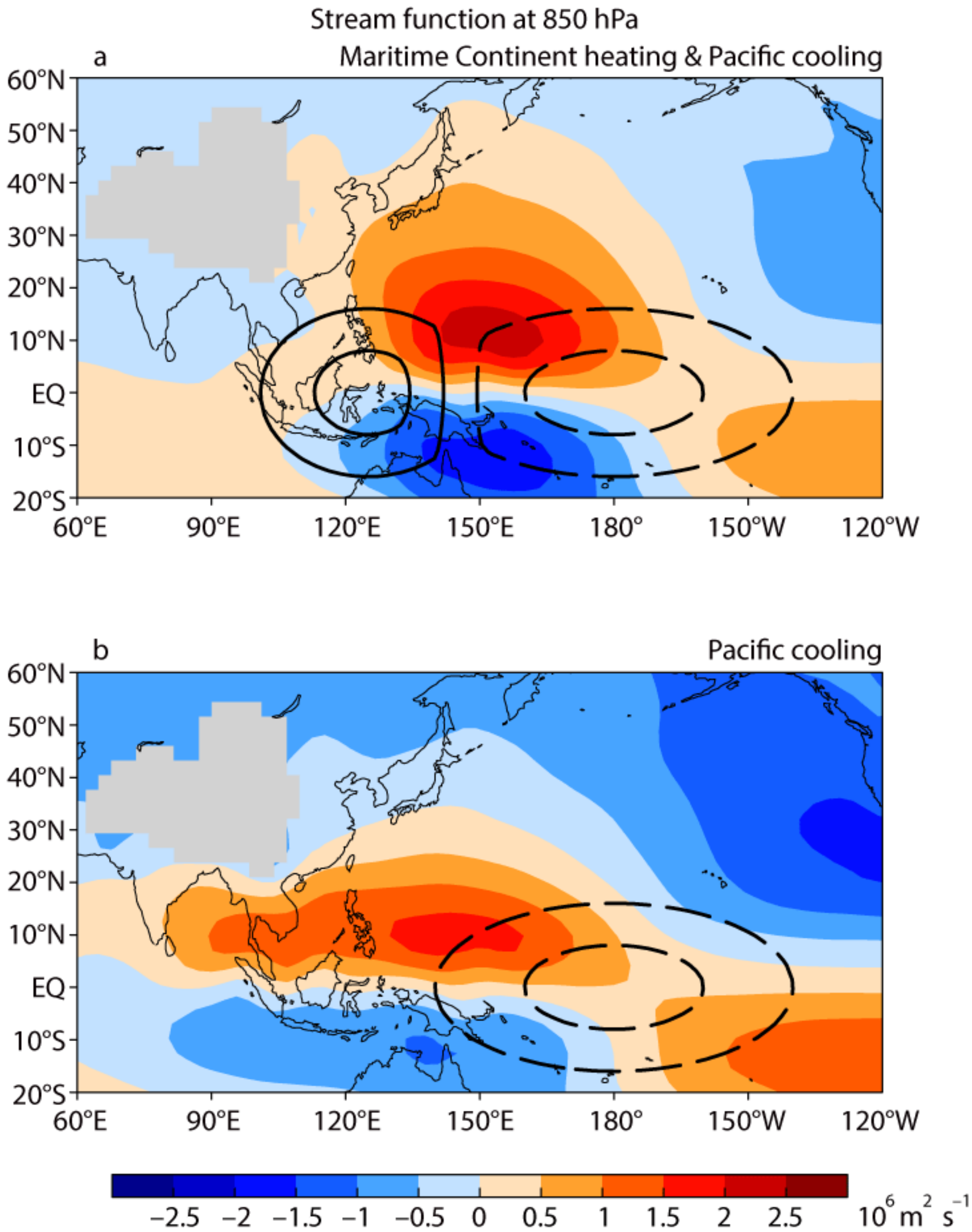


Fig. 7. Atmospheric response to tropical diabatic heating simulated with Linear Baroclinic Model. (a) Atmospheric response to the Maritime Continent heating and the Pacific cooling found in El Niño-to-La Niña transition years (Fig. 4g). (b) Atmospheric response to the Pacific cooling. Shading indicate stream function at 850 hPa ($10^6$ $m^2$ $s^{-1}$). Dashed and solid contours indicate prescribed cooling (–0.6 and –0.2 K $day^{-1}$) and heating (0.2 and 0.6 K $day^{-1}$) at 454 hPa, respectively.